Chemical Science

ROYAL SOCIETY OF CHEMISTRY

PERSPECTIVE

View Article Online
View Journal | View Issue

Cite this: *Chem. Sci.*, 2025, **16**, 18504

All publication charges for this article have been paid for by the Royal Society of Chemistry

Received 31st July 2025
Accepted 25th September 2025

DOI: 10.1039/d5sc05791d

rsc.li/chemical-science

Emerging flexible heterojunctions: fabrication, properties and optoelectronic applications

Meiqi Dai and Dongpeng Yan *

Flexible heterojunctions have attracted increasing attention in recent years due to their multifunctionality and exceptional advantages for optoelectronic applications, such as mechanical compliance, dimensional freedom and strain tunability. With the rapid development of flexible heterojunctions, a comprehensive view of assembly strategies for their generation and regulation with precise control is highly desirable. In this perspective, we systematically summarize recent key advances in flexible heterojunctions from various aspects, including their classification, assembly strategies and representative applications. We also highlight the effect of the underlying structure–property relationship on the performance of flexible heterojunctions, particularly in systems of small molecules, polymers and inorganic–organic hybrids. Our aim is to bring together pieces of research from fundamental discoveries of flexible heterojunctions to their properties under different application backgrounds. Finally, we propose the current issues and future trends to provide new ideas for continuous improvement in this field.

1. Introduction

The assembly and application of heterojunctions have garnered increasing academic and industry attention based on their combination of multifunctionality for miniaturized devices.[1–8] Integrating two or more different solid interfaces can generate novel optoelectronic performance compared to their individual components.[9–11] The early manufacturing strategy for heterojunctions with a lattice-matched interface generally involved chemical epitaxial growth or physical vapor deposition.[12–15] In recent years, heterojunction materials such as two-dimensional (2D) van der Waals heterojunctions[16] and perovskite heterojunctions[17–20] have been well developed, which offer alternative assembly methods through van der Waals integration and solution processing. In a broader context, the term "heterojunctions" refers to interfaces formed by dissimilar materials including amorphous and crystalline forms, whether they are formed through doping engineering or stimulus-responsive fabrication.[16,21] Over the past two decades, a variety of strategies have been developed to generate heterojunctions for optoelectronic applications from flexible materials. Until now, flexible heterojunctions with diverse morphologies have

Key Laboratory of Radiopharmaceuticals, Ministry of Education, College of Chemistry, Beijing Normal University, Beijing, China. E-mail: yandp@bnu.edu.cn

Meiqi Dai

Meiqi Dai obtained her bachelor's degree in 2020 and master's degree in 2023 from Beijing Normal University. She is currently working on her PhD at Beijing Normal University under the supervision of Prof. Dongpeng Yan. Her research interests mainly focus on designing flexible molecular-based materials and exploring photonic information applications.

Dongpeng Yan

Prof. Dongpeng Yan received his PhD degree from the Beijing University of Chemical Technology (BUCT) in 2012 and then became an associate professor at BUCT. In 2014, he moved to BNU as a full professor. From 2011 to 2013, as a visiting student/scholar, he studied at the Department of Chemistry, University of Cambridge, and School of Pharmacy, University College London. He is a Royal Society of Chemistry Fellow (FRSC). His research interests focus on materials chemistry, luminescence, and photocatalysts.

been controllably synthesized, including multiblock, circular shape, branch type, network, and so on.[22–25]

The hot topics and advantages involved in the research on flexible heterojunctions are summarized as follows: (1) Mechanical compliance: the newly realized mechanical flexibility renders heterojunctions capable of conformability, bendability and stretchability.[26,27] (2) Band engineering: geometrically, the tunable distance between adjacent components contributes to adaptable carrier transport length and controlled electron–hole wavefunction overlap.[28] Band alignment has a significant impact on the optoelectronic applications of heterojunctions. For example, the straddling-type band structure enables efficient collection of photo-generated carriers, which is suitable for LEDs and photodetectors. The staggered-type band structure facilitates the effective transition of photo-generated electrons, making it applicable to phototransistors and photocatalysis. (3) Dimensionality freedom: dimensional transformation from one to two and three enables additional freedom to engineer charge carriers/excitons and band gaps. (4) Strain tunability: flexible heterojunctions integrate dissimilar materials into a bendable system, which could keep structural and functional integrity against diverse deformations, enabling them to have crack tolerance and durability. (5) Application extensibility: compared with ordinary rigid heterojunctions, flexible materials embed multiple functionalities such as sensing, processing and response, which expand the scope of heterojunction materials for applications such as smart skins, robots, and biomedical devices.[29,30]

However, to date, profitable flexible heterojunctions are not readily available, and key issues need to be settled, such as how to construct heterojunctions with desired flexibility from the microscale molecules to the macroscopic device. Consequently, a systematic summary and timely account to accelerate the development of this emerging and challenging field are necessary. In this perspective, we will give a comprehensive overview of flexible heterojunctions from the molecular scale to the macroscale for flexible optoelectronics. More specifically, we first introduce intrinsically and structurally flexible heterojunctions from crystals, polymers and composites at the componential level. Next, we systematically summarize detailed synthetic strategies in flexible heterojunctions from the perspective of statically programmable bottom-up assembly and the dynamically reprogrammable macromanipulation approach. We also demonstrate multifunctional properties and some representative optoelectronic applications (Scheme 1). Finally, we propose a comprehensive conclusion and forward-looking perspectives on the future challenges and research trends in this fascinating field.

2. Classification

The cornerstone of flexible optoelectronics is the realization of materials with mechanical compliance and advanced optoelectronic properties.[31–35] To realize favorable mechanical compliance of heterojunctions, molecular design and geometric engineering are two common scenarios. The former focuses on developing novel materials with intrinsic flexibility, while the latter relies on integrating rigid materials in specific geometric forms. In general, flexible heterojunctions can be divided into intrinsically flexible heterojunctions and structurally flexible heterojunctions, respectively (Fig. 1).

2.1 Intrinsically flexible heterojunctions

Intrinsically flexible heterojunctions are composed of materials with inherent flexibility, which are mainly polymers and flexible crystals. The inherent flexibility originates from molecular-level deformations, such as rotation of chemical bonds, switching of halogen or hydrogen bonds, conformational transitions, molecular chain sliding and dynamic bond formation.[36–41] These materials exploit inherent elasticity or plasticity to withstand diverse deformations, exhibiting mechanical flexibility

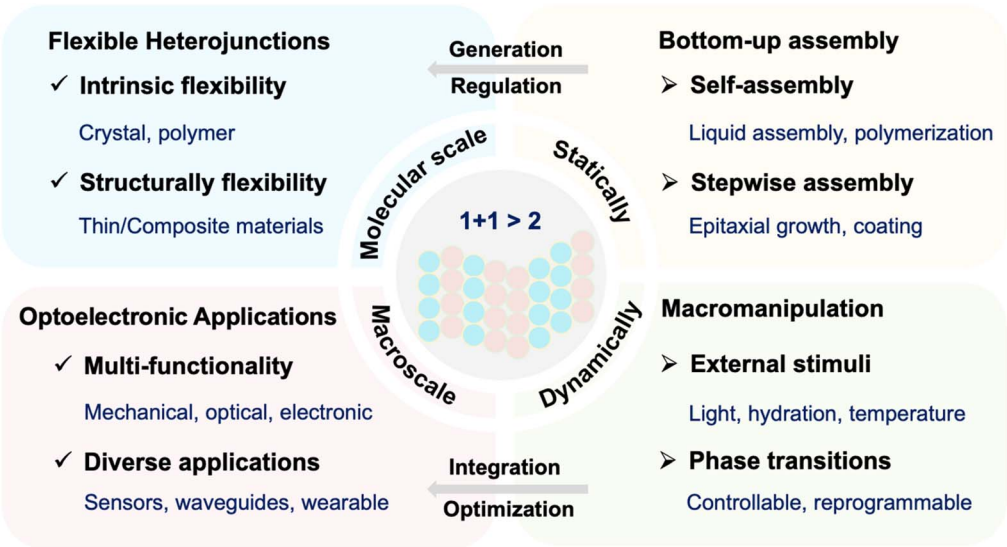

Scheme 1 Assemblies, methods and applications of flexible heterojunctions.

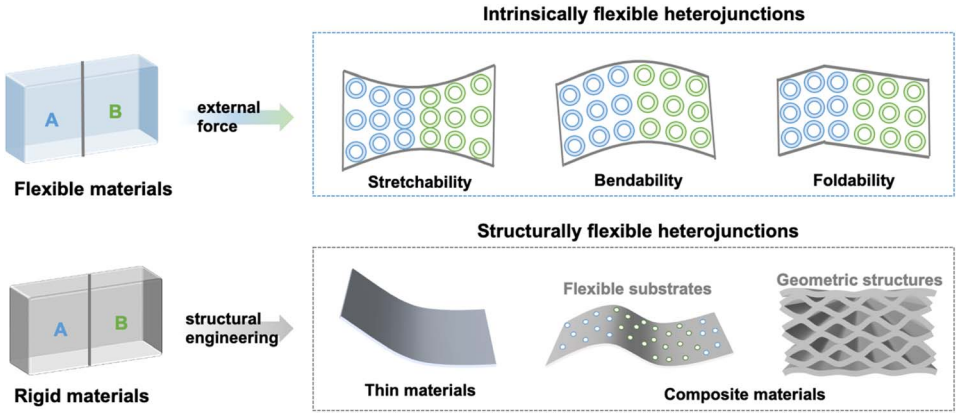

Fig. 1 Schematic diagrams of intrinsically flexible heterojunctions and structurally flexible heterojunctions.

including stretchability, bendability, and foldability from the microscale to the macroscale. The optoelectronic functionality persists under deformation due to nano-scaled strain accommodation mechanisms, making them ideal for applications such as flexible optical waveguides and flexible sensors.

2.2 Structurally flexible heterojunctions

Structurally flexible heterojunctions are composed of traditional rigid materials, which achieve flexibility through structural engineering, including thin materials and composite materials. For thin materials, according to Euler–Bernoulli beam theory, reducing the thickness can impart bending capability to originally rigid materials.[42,43] For composite materials, one approach involves regularly arranging rigid heterojunctions on flexible substrates, *e.g.*, utilizing microfabrication techniques to deposit nanostructures onto flexible polymer substrates to form flexible arrays. Another method is primarily relying on the design of geometric structures, such as buckled, wrinkled or kirigami structures.[44–47] The heterojunctions may remain intrinsically brittle. Structurally flexible heterojunctions could decouple optoelectronic performance from mechanical resilience, enabling high-efficiency application such as wearable devices on bendable platforms.

3. Bottom-up assembly

The controllable fabrication of heterojunctions using flexible materials or flexible substrates is a primary objective. The bottom-up assembly method refers to the construction of heterojunctions by starting from small components or building blocks to larger structural units. This method enables heterojunctions with embedded growth interfaces together with high spatial and angular precision. To synthesize flexible heterojunctions with precise control, in-depth understanding of the corresponding pathway complexity and efficient tuning of various kinetic and thermodynamic aggregates of different components are crucial. In this section, we will systematically describe the different types of flexible heterojunctions and their corresponding preparation methods, such as the self-assembly and stepwise layer-by-layer assembly of sequential flexible heterojunctions. The materials include intrinsically flexible crystals, polymers, structurally flexible thin materials and composites. While direct assembly offers simplicity of preparation, the stepwise layer-by-layer assembly provides the opportunity for fine control over the multilayer structure of the heterojunctions.[48–51] Furthermore, we will also demonstrate the representative optoelectronic applications based on these fabricated flexible heterojunctions.

3.1 Crystal based heterojunctions

Crystalline compounds have been successfully developed as flexible heterojunctions, which mainly include organic crystals, organic metal halides and inorganics with a colloidal axial superlattice.[52] Most of the reported flexible crystals initially exhibit one-dimensional morphology (such as needle-like, rod-like or ribbon-like), and those crystal-based flexible heterojunctions can be transformed into diverse morphologies, including multiblock, circular shape and branch type. The flexibility of these crystals is implemented by regulating intermolecular interactions and crystal stacking/arrangement patterns.[31,53–59] Furthermore, the complex structure of crystal-based flexible heterojunctions offers the possibility to finely manipulate spatial excitonic emission along the path of light propagation, thereby enabling multichannel and multiband photoemission performance.

Liquid self-assembly, favored for fabricating organic crystal flexible heterojunctions due to its simplicity and scalability, enables tuning of crystal form and size by adjusting solvent conditions. Moreover, introducing an antisolvent (or poor solvent) can regulate nucleation and crystal growth rates, thereby facilitating stepwise crystallization and heterojunction formation through solvent evaporation. In 2023, Zhao *et al.*[60] proposed a surface tension-assisted heterogeneous self-assembly strategy to construct hetero-microrings. 9,10-Dicyanoanthracene (DCA) molecules were utilized as the host crystals for constructing microrings due to their good bending stress during the growth process of curved structures (Fig. 2a and b). Under ultrasonic oscillation, DCA units in dichloromethane solution are quickly injected into ultrapure water to create an oil-in-water emulsion, which is then drop-cast

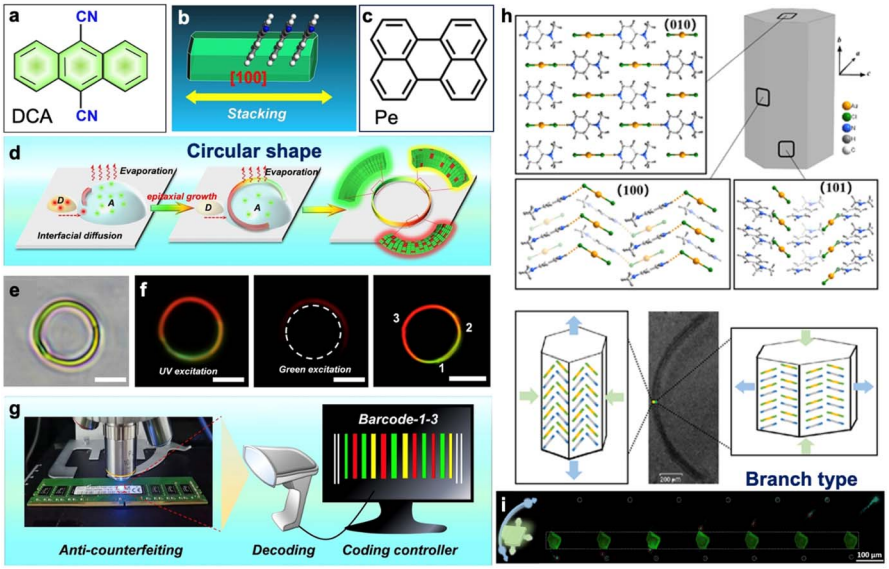

Fig. 2 (a) Molecular structure of DCA. (b) Simulated growth morphology of DCA molecules. (c) Molecular structure of Pe. (d) Schematic illustration of construction of hetero-microrings whose heterogeneous nucleation and growth were controlled by the directional diffusion between the hetero-emulsion droplets. (e) Bright-field microscopy images of the hetero-microrings. (f) PL images of a typical hetero-microring excited using UV light and green light bands, respectively. And a PL image of a typical hetero-microring excited at positions of 1–3. (g) Demonstration of hetero-microring-based photonic barcodes for advanced anti-counterfeiting of an electronic component. All scale bars are 5 μm. (h) Crystal structure and the elastic bending mechanism of Au–DMAP. (i) Optical waveguide performances of the heterojunction by exciting with a 375 nm laser beam. Reproduced with permission from (a–g) ref. 60 (copyright 2023, John Wiley and Sons) and (h and i) ref. 64 (copyright 2023, Science Partner Journal).

on glass. As the solvent evaporates, DCA molecules nucleate at the interface and assemble into ring-shaped structures due to surface tension. By doping perylene (Pe) molecules (Fig. 2c) with strong electron-donating abilities into DCA host microcrystals, the emissive color can be tuned from green to red through adjusting Pe doping content. Furthermore, injecting donor (D: Pe) and acceptor (A: DCA) molecules separately into a poor solvent under ultrasonic vibration leads to the formation of hetero-microrings with inhomogeneous spatial composition and multicolor emission, due to preferential nucleation of CT complexes at the contact interface between hetero-emulsion droplets (Fig. 2d–f). Based on the coding rule from the multi-color heterorings, the barcodes 1, 2, and 3 can be acquired using an encoder. These obtained multicolor microrings offer a versatile platform for encoding abundant information, which was further used for anti-counterfeiting (Fig. 2g).

The seeded epitaxial growth method has emerged as an effective strategy for preparing organic metal halide hetero-junctions, relying on similar lattice constants between two crystals.[61–63] The fabrication process involves the first seed crystal synthesis, interface dissolution and the second crystal epitaxial growth on the surface of the first crystal. In 2023, our group[64] fabricated branch-type flexible heterojunctions through an epitaxial-growth method based on 1D flexible microrods and 2D microplates. First, new types of 0D organic metal halides were synthesized using 4-dimethylaminopyridine (DMAP) as a phosphor unit with metal halides AuCl and $MnCl_2$ *via* both hydrothermal and solvent volatilization methods. Next, Au–DMAP can be bent under external mechanical stress with an elastic strain of 8.02%. After releasing the external stress, the crystals can quickly return to their original straight shape. We suggested that the high elasticity of flexible Au–DMAP crystals originates from the buffer regions in the crystal structure, formed by the N–H···Cl hydrogen bond, molecular stacking and electrostatic interactions (Fig. 2h). The lattice mismatch ratio value between Au–DMAP and Mn–DMAP at the interface can be calculated as low as 3.3%, which is advantageous for the nucleation and epitaxial growth of Mn–DMAP on the side of Au–DMAP to form heterojunctions. Therefore, we have successfully prepared branch type flexible heterojunctions. Au–DMAP was initially grown as trunks, and then a saturated Mn–DMAP solution was added onto these trunks, leading to the epitaxial growth of microplates on the microrods' side surfaces. The novel heterojunction demonstrates flexible optical waveguides with multiple photonic output ports (Fig. 2i). Under a focused 375 nm laser beam, the photonic signal in the heterojunction could transfer to 2 opposite directions around the 1D microrod and 2D microplate. In addition, by changing the excitation site, the luminescence color of each pot could be changed.

Compositionally, the large lattice-mismatch tolerance in axial superlattice nanowires allows vast material combinations and offers a fertile ground for engineering such hetero-structures with flexibility.[65,66] In 2024, Yu *et al.*[67] demonstrated an under-stoichiometric reaction strategy towards solution-synthesized 1D segmented heterostructures. Te nanowires with a high aspect ratio were selected as the model structural unit. After adding under-stoichiometric Ag^+ and complexing agent NH_4SCN to dramatically decelerate the reaction in the

aforementioned solution, Te/Ag_2Te with a segmented heterogeneous nanostructure was fabricated (Fig. 3a and b). Te and Ag_2Te form their lattices independently (Fig. 3c and d), and the segment control can be achieved with variations of Ag feeding. The segments close to each other attract and merge into a continuum, while the segments far away repel each other, finally forming the segment Te/Ag_2Te. Mechanical simulations suggest the three-stage (Fig. 3e) kinetic evolution from Te nanowires to Te/Ag_2Te heterostructures: the initial Ag_2Te island is embedded into Te templates with a very small size (Fig. 3f). As the reaction processed, the islands grew larger and became more numerous; subsequently, some islands began to permeate throughout the diameter, forming stripped structures. It is worth noting that the stress caused by the embedded Ag in the front of the island is tensile, while the sides are compressive, which promotes radial growth for the Ag_2Te island (Fig. 3g). Te and Ag_2Te segments both experience elastic energy-driven ordering. Ag^+ migration causes the interface between Te and Ag_2Te to move, forming the segmented structure with uniform length distribution (Fig. 3h). Due to the large driving force, even the large mismatch strain facilitates the coalescence of the adjacent segments. Using this broad strategy, more well-controlled axially segmented heterostructures were fabricated by changing metal cations.

3.2 Polymer based heterojunctions

Polymers, with their abundant molecular availability, solution processibility and inherent flexibility, have attracted much interest and are mainly synthesized through crosslinking of precursor molecules.[68–70] Owing to a rough blending interface with less-ordered molecular packing, polymer-based flexible heterojunctions could exhibit distinct properties compared to typical crystalline materials mentioned above. Furthermore, different raw materials exhibit distinct characteristics (such as molecular weight, hydrophilicity and structural designability) and crosslinking mechanisms (such as covalent bonds, adaptive covalent bonds and non-covalent bonds).[71–74] Bottom-up assembly exploits kinetics or thermodynamics to autonomously organize different polymers into heterojunctions. As the diversity of synthesized polymers continues to expand, the interactions between macromolecules have become important to explain the materials' properties at the molecular scale. The selection of polymers will influence the processability and functions of heterojunctions.

3.2.1 Polycrystalline polymers. Polycrystalline polymer heterojunctions follow a superlattice framework in periodic geometry but have a heterojunction interface created by fine-tuned solvent corrosion. The backbone mainly relies on covalent crosslinking; meanwhile, its relatively ordered molecular

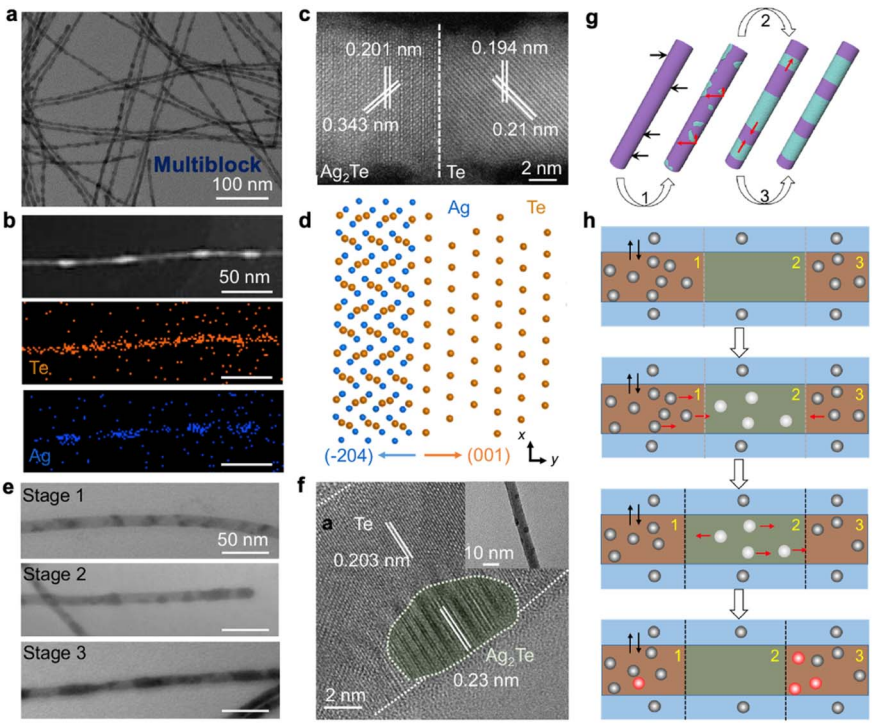

Fig. 3 (a) Transmission electron microscopy (TEM) image of the segmented periodic heterostructure. (b) High-angle annular dark field (HAADF) and energy dispersive spectrometer (EDS) mapping of the homogeneous distribution of Te (orange) and heterogeneous distribution of Ag (blue). All scale bars are 50 nm. (c) High-resolution transmission electron microscopy (HRTEM) image of the specific interface between Te and Ag_2Te. (d) A schematic atomic model, specifying an atomically sharp interface in heterostructures. (e) Time-resolved TEM images. $t = 10$ s, 30 s and 3 min for Stage 1, 2, and 3, respectively. t is the reaction time between Te and Ag^+. (f) HRTEM image of the island on the nanowires. Inset: a TEM image of the nanostructure formed at the beginning. (g) Schematic illustration of three stages involved in the evolution of the periodic heterostructure. (h) Schematic diagram of the interface movement in the segmented nanowires imposed by Ag migration. The blue columns represent the Ag^+ solution surrounding the nanowires, while the brown and olive columns represent Ag_2Te and Te segments, respectively. Reproduced with permission from (a–h) ref. 67 (copyright 2024, Springer Nature).

packing assists crystallization. Di and Zhao *et al.*[75] proposed a polymeric multi-heterojunction (PMHJ) with periodic dual-heterojunction features using sequential assembly. They selected and utilized selenium-substituted diketopyrrolopyrrole (PDPPSe-12) and poly(2,5-bis(3-tetradecylthiophen-2-yl)thieno[3,2-*b*]thiophene) (PBTTT) as individual polymers (Fig. 4a–c). PDPPSe-12 or PBTTT solution with varying concentrations of 4Bx was spin-cast to form a film, which was then subjected to a photocrosslinking process. 4Bx (a four-armed azide-based crosslinker) was blended to crosslink the film to inhibit the aforementioned solvent corrosion and manipulate interfacial properties during multiple sequential coating processes (Fig. 4d). By combining all mass intervals of the film using time-of-flight secondary ion mass spectrometry (TOF-SIMS), alternating layers with PDPPSe-12, PBTTT and the interface were constructed. The PMHJ was indexed as (L_{P1}, L_I, L_{P2}), where L_{P1}, L_I and L_{P2} are the thicknesses of PDPPSe-12, the interface and the PBTTT layer, respectively. With the introduction of a 4Bx amount of ≥2 wt%, the thickness of PDPPSe-12, PBTTT and the interface layer was found to be 6.3 ± 0.5 nm, 4.2 ± 0.4 nm and 3.9 ± 0.4 nm (Fig. 4e–h), respectively, which corresponds to 2–3 molecular layers. The periodic number can be extended to 100, resulting in a maximum thickness of over 1800 nm to satisfy diverse thickness requirements. Moreover, the interface shows a gently interpenetrated network, which is the characteristic bulk heterojunction feature. The PMHJ structure is compatible with solution coating techniques, satisfying the demand for ultraflexible plastic materials towards cost-effective wearable thermoelectrics.

3.2.2 Programmable vitrimers. Programmable vitrimers represent a promising type of smart polymeric material characterized by their adaptive covalent networks, which exhibit tunable mechanical properties and shape memory.[76–79] The chemical network design generally depends on switchable polymer segments, such as those exhibiting glass transitions or melting cyclization. Generally, a heterojunction is shown to be highly dependent on the topological match of the donor and acceptor polymers; in this case, introducing a dispersion phase can enhance the network reconfiguration of the vitrimer. Liu *et al.*[80] introduced an orthogonal polymerization-induced phase-engineering strategy to fabricate vitrimer heterogel (VHG) materials. The fabricated heterogel materials involved a stiff vitrimer framework phase (VFP) and soft ion-liquid gel framework phases (IFPs). The VFP is formed by a polyurethane reaction between poly(caprolactone) diol (PCL-diol) and trifunctional hexamethylene diisocyanate (THDI), and IFPs are

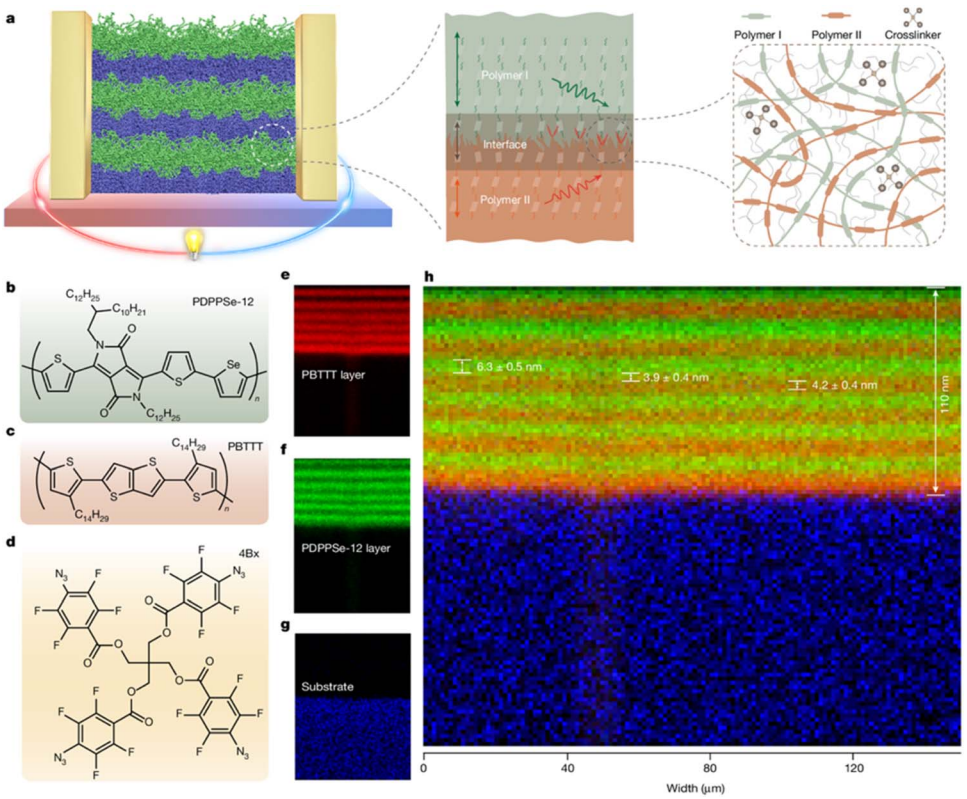

Fig. 4 (a) Illustration of the PDPPSe-12:PBTTT PMHJ film. The PDPPSe-12 and PBTTT layers are depicted in blue and green, respectively. The colon in PDPPSe-12:PBTTT stands for a sequentially processed periodic film. PDPPSe-12 and PBTTT were photo-crosslinked by 4Bx. (b–d) Chemical structures of PDPPSe-12 (b), PBTTT (c) and the crosslinker 4Bx (d). (e–g) TOF-SIMS cross-sectional images along the *y*–*z* axis of a single PDPPSe-12:PBTTT PMHJ (six period) film. The characteristic signals of the PDPPSe-12 layer (e; red), the PBTTT layer (f; green) and the substrate (g; blue) were extracted and reconstructed using software. (h) The overlay of TOF-SIMS cross-sectional images of PDPPSe-12 (e), PBTTT (f) and the substrate (g). The periodic thicknesses are calibrated using a step profiler and STEM-EDS measurements. Reproduced with permission from (a–h) ref. 75 (copyright 2024, Springer Nature).

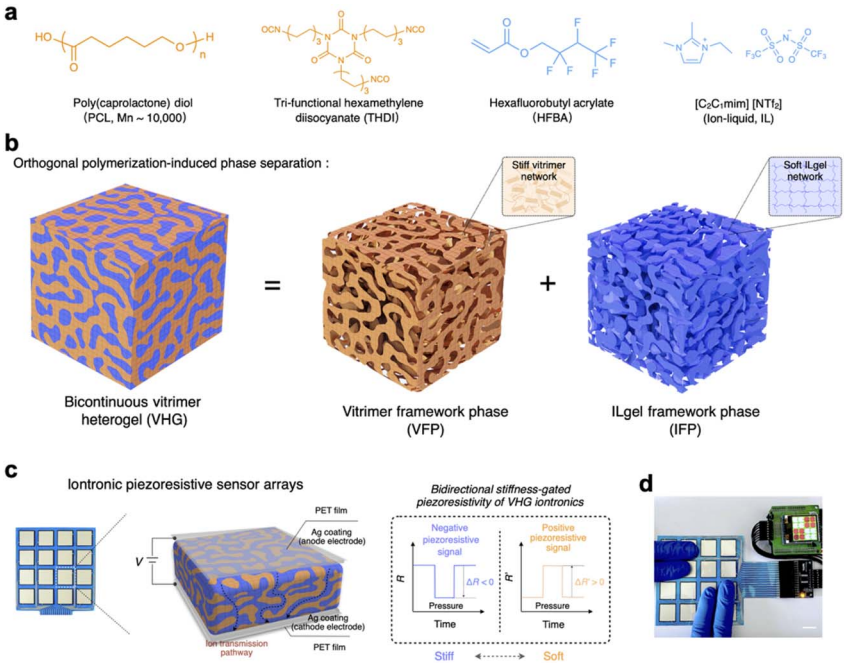

Fig. 5 (a) Chemical structures of reacted precursor components within VHGs. (b) VHGs have the bicontinuous structure of VFP and IFP framework phases owing to orthogonal polymerization-induced phase separation. (c) Schematic illustration of VHG iontronic piezoresistive sensor (4 × 4) arrays that had the capability of bidirectional stiffness-gated piezoresistivity. Scale bar, 1 cm. (d) When the VHG iontronic sensor units were pressed, the corresponding feedback was reflected on the monitor. Reproduced with permission from (a–d) ref. 80 (copyright 2024, American Association for the Advancement of Science).

derived from an ultraviolet free-radical polymerization of hexafluorobutyl acrylate (HFBA) (Fig. 5a). By applying UV light and heat simultaneously, the gelation point of the VHG rapidly occurred. The VFP and IFPs underwent phase separation during this "one-step" orthogonal polymerization process, leading to the gradual formation of the VHG bicontinuous structure. Besides, the VFP component, as a stable individual phase within the VHG, cannot be affected by the solvation effect of the IFP component (Fig. 5b). The VHG exhibited high mechanical strength and stretchability, which was attributed to the coordination effects of the bicontinuous "softness" and "stiffness" phases and interfaces. For example, when the weight ratio of the VFP to the VHG was 7.5, the VHG yielded a stiff elastic modulus of 116 MPa and could withstand a stretchable deformation up to 600%. Moreover, above its melting temperature, the softened VHG could be programmed to a temporary shape *via* stretching. When the VHG was cooled below melting temperature, the VFP crystallized, thereby solidifying the VHG's temporary shape. Interestingly, by repeating the process, the shape could be programmed into other shapes like origami or kirigami. Based on the soft and stiff states, bidirectional stiffness-gated positive and negative piezoresistivity sensors can be achieved. In the stiff state, the VHG sensor showed negative piezoresistivity, whereas in a soft state, the sensor demonstrated a positive piezoresistivity (Fig. 5c and d).

3.2.3 Supramolecular copolymers. Supramolecular polymers, based on small molecules held together by directional and reversible non-covalent forces, display dynamic and flexible monomer-to-polymer transitions. Their intrinsic self-organizing properties offer the possibility of creating finely tuned multi-functional copolymers.[81–85] Block copolymers are molecules in which polymer chains of different chemical compositions are attached at a common junction. In this context, the attractive bottom-up synthetic strategy of living seeded supramolecular polymerization motivated progress in developing flexible axial heterostructures with controlled sequences. In 2020, George *et al.*[86] reported supramolecular block copolymerization in solution under thermodynamic control for the synthesis of axial organic heterostructures. This strategy requires two structurally similar monomers to minimize the structural mismatch. By attaching ethoxy (–OEt) and pentanethiol ($-SC_5H_{11}$) core-substituted naphthalene diimide (cNDI) derivatives to chiral (*S*,*S*)-*trans*-1,2-bis(amido)-cyclohexane motifs, green fluorescent SS-diOEt and red fluorescent SS-dithiol monomers were fabricated (Fig. 6a and b). Compared to SS-dithiol fiber, SS-diOEt fiber demonstrated more defects, where monomers can exchange in/out of the stacks, leading to the dynamic mixing of monomers. Therefore, the two components were co-assembled when a 1 : 1 mixture of SS-diOEt and SS-dithiol in 25% tetrachloroethane and methylcyclohexane was heated to 363 K and cooled to 298 K (Fig. 6c) at a rate of 1 K min^{-1}. The supramolecular block copolymerization process from the monomeric state of components follows a nucleation–elongation mechanism, which means the heterogeneous nucleation of SS-diOEt on SS-dithiol nuclei. The blocky organization of the components in the axial heterostructures is determined by the reactivity ratio of monomers.

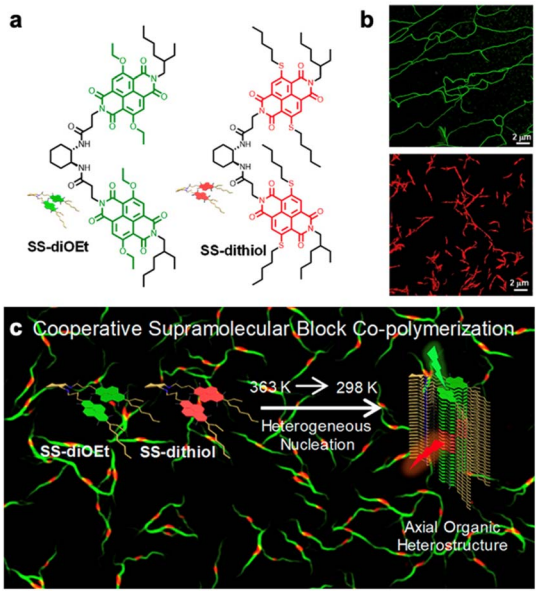

Fig. 6 (a) Molecular structures of SS-diOEt and SS-dithiol monomers along with a schematic. (b) SEM images of green (green channel) and red (red channel) fluorescent 1D supramolecular homopolymers for SS-diOEt and SS-dithiol, respectively. (c) Schematic representation of light-harvesting axial organic heterostructures with green-red-green segmented microstructures. Reproduced with permission from (a–c) ref. 86 (copyright 2020, American Chemical Society).

Furthermore, amplification in SS-dithiol (energy acceptor) emission along with the quenching of SS-diOEt (energy donor) emission indicates energy transfer between donor–acceptor block segments.

3.3 Thin material based heterojunctions

2D layered materials, for instance, graphene, hexagonal boron nitride (hBN), transition metal dichalcogenides (TMDs), transition metal oxides (TMOs), transition metal carbides, nitrides and carbonitrides (MXenes) and new emerging materials, are bonded by relatively weak van der Waals interactions between their layers. This makes it possible to isolate, mix and match atomic layers with different heights, thereby facilitating the creation of van der Waals heterostructures. Moreover, without the constraints of lattice matching and processing compatibility, this strategy is suitable for the flexible integration of different materials with distinct dimensions (Fig. 7a).[87–89] Compared to rigid three-dimensional materials, flexible low-dimensional materials or thin films possess better flexibility and deformability. And they are more appropriate for van der Waals integration.

Currently, exfoliation is a widely used method for obtaining high-quality 2D thin materials. However, residual impurities on the material surface are hard to avoid during the exfoliation process. Moreover, the techniques for interfacial engineering during the assembly of heterostructures remain underdeveloped, resulting in challenges in achieving atomic-level crystal alignment between layers and thereby introducing interfacial defects. To address these challenges, Cho *et al.*[90] fabricated patterned van der Waals heterostructures from electrochemically exfoliated 2D layers using a photoreactive crosslinker. First, they selected insulating HfO_2, semiconducting MoS_2 and metallic graphene as the dielectric layer, the channel and electrodes, respectively (Fig. 7b). Then they prepared these layers by molecular intercalation-based electrochemical exfoliation. Polyvinylpyrrolidone (PVP) was added to stabilize the 2D nanosheet in chloroform, which remained as a residual surfactant after purification. Subsequently, under UV light irradiation, the introduced photoresponsive crosslinker ethane-1,2-diyl bis(4-azido-2,3,5,6-tetrafluorobenzoate) can generate a reactive singlet nitrene intermediate ($^{-1}$N). And the reactive $^{-1}$N can readily undergo a C–H insertion reaction with the alkyl chains of the residual PVP to form a crosslinking network at the interfaces of the 2D nanosheet (Fig. 7c). Finally, this crosslinker-based direct photopatterning strategy increased the mechanical stability of the 2D layers and was widely applicable to various 2D materials and various patterns (Fig. 7d). This strategy can be used to fabricate a field-effect transistor through multi-stacking integration of insulating HfO_2, semiconducting MoS_2 and metallic graphene (Fig. 7e). Specifically, HFS_2 nanosheets and the crosslinker mixture in chloroform were spin-coated onto a heavily doped Si substrate. Then the as-deposited film was exposed to UV light using a photomask and ultrasonicated in fresh chloroform to remove the uncrosslinked regions, which were converted into HfO_2 at 500 °C for 5 h. And each dispersion of MoS_2/graphene and crosslinker mixture in chloroform was processed similarly onto the prepatterned layer to form stacked van der Waals heterostructures.

3.4 Composite based heterojunctions

Leveraging the optoelectronic properties and mechanical compliance of heterojunctions and flexible substrates, flexible heterojunctions based on composite materials have enabled diverse applications across multiple disciplines. Their performance and scope of utility underscore the significant technological potential arising from the synergistic combination of desirable attributes.

A promising strategy for designing flexible heterojunctions based on composite materials involves the integration of rigid heterojunctions onto flexible substrates,[91,92] typically achieved through microfabrication techniques that deposit nanostructures onto polymeric substrates, thereby creating mechanically compliant yet functionally enhanced arrays. In 2020, Peng *et al.*[93] presented a new class of ZnS/CaZnOS heterojunctions. The mechanoluminescence (ML) intensity is ≈2.2 times higher than that of commercial ZnS and 3.5 times higher than that of commercial CaZnOS. They prepared ZnS/CaZnOS heterostructures by a decomposition–combination reaction between $CaCO_3$ and ZnS in an Ar atmosphere at 1100 °C for 4 h. Elemental mapping reveals that the final product is indeed composed of ZnS/CaZnOS heterostructures rather than a simple mixture of ZnS and CaZnOS (Fig. 8a and b). Furthermore, Mn^{2+} ions (1 mol%) were selected as a model dopant to substitute for Zn^{2+} in both the ZnS and CaZnOS phases. The Mn element was detected in all parts of the particles, indicating the

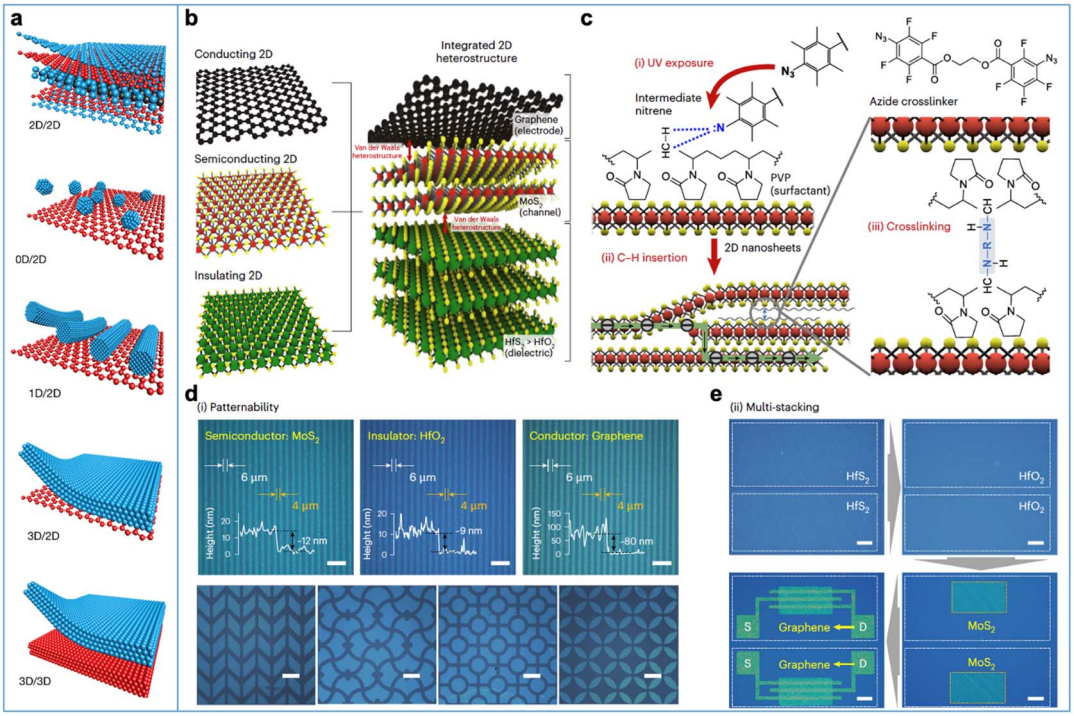

Fig. 7 (a) Schematic illustrations of 2D/2D integration and vdW integration beyond 2D materials. (b) Schematic illustration of the 2D materials and van der Waals heterostructure assembled with metallic graphene, semiconducting MoS_2 and insulating HfO_2 (oxidized from HfS_2). (c) Schematic description of the photo-crosslinking process between neighboring 2D nanosheets based on the C–H insertion reaction with PVP surfactants. (d) Optical microscopy images of various 2D van der Waals patterns fabricated by direct photopatterning. (e) Optical microscopy images of the fabrication procedures for the 2D material-based FETs. Scale bars, 30 μm (c, top row), 500 μm (c, bottom row), and 200 μm (d). D, drain; S, source. Reproduced with permission from (a) ref. 87 (copyright 2019, Springer Nature) and (b–e) ref. 90 (copyright 2025, Springer Nature).

incorporation of Mn into both ZnS and CaZnOS phases (Fig. 8c). Subsequently, based on the aforementioned work, in 2023, Peng *et al.*[94] built a multimode sensing platform combining a ZnS/CaZnOS:Mn^{2+} heterojunction using a 3D-printing technique and fiber spinning, which triggered heterojunctions with flexibility (Fig. 8d). Employing the high-temperature solid-state method through a combination of $Zn_{0.99}S$:0.01Mn^{2+} and $CaZn_{0.99}OS$:0.01Mn^{2+}, the ZnS/CaZnOS:Mn^{2+} heterojunction was synthesized. When the heterojunction powder is introduced into a polymer host (including a 3D-printed polymer or cellulose fibers), the ML can still be observed. The pure polymer only exhibits a blue emission under 365 nm UV light irradiation (Fig. 8e), whereas the modified polymer demonstrates orange emission observed through a long pass filter (Fig. 8f). It is worth noting that the folded shape of the fabricated composites amplified the ML effect when the surface is rubbed with metal items, plausibly due to an even distribution of the heterojunction in the polymer and high flexibility of the 3D-printed materials. The developed 3D-printed ML-active polymer also allowed low-temperature sensing from a few to ≈100 bar, a range previously inaccessible by any other optical sensing technique. Furthermore, the multimode sensing platform working as a stress sensor can be knitted into fabrics showing intense ML signals for further potential in wearable devices (Fig. 8g and h).

Another effective method involves geometric structural design to impart flexibility or tunable mechanical properties to otherwise rigid materials. In 2022, Rotenberg *et al.*[95] created a pure-silicon porosity-based heterojunction by combining self-limiting stain etching and a high-power oxygen plasma treatment. The porous surface can create a softer interface (Fig. 9a). Stain etching is a type of electroless etching enabled by hole injection from strong oxidants in solution into the valence band, which can produce different types of porous structures on the surface of silicon. Oxidation of the nanoporous silicon may mitigate the mechanical impact of the structural defects in silicon by introducing the atomic-scale or nanoscale oxide phase. Nanoporous/non-porous silicon heterojunctions were generated in p-type crystalline silicon using metal-free etching with hydrofluoric acid and nitric acid. The micropillars on the surface of the silicon formed during etching may contribute to enhanced photoelectrochemical properties through increased surface light trapping (Fig. 9b and c). Besides, STEM images showed a sharp interface between nanoporous and non-porous domains in the pure-silicon heterojunction (Fig. 9d). This coherent single-crystal structure yields efficient charge transport due to the absence of amorphous regimes. The fabrication approach is also compatible with the processing of ultrathin, soft and flexible silicon membranes fabricated from silicon-on-insulator substrates. The fabricated flexible crystalline silicon

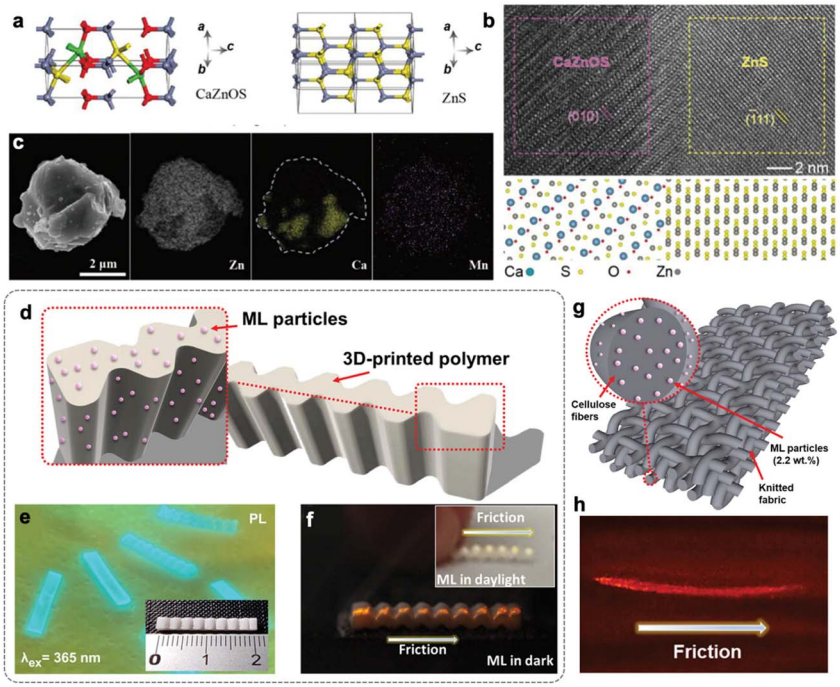

Fig. 8 (a) Schematic presentation of CaZnOS and ZnS structures, respectively. (b) High-resolution TEM image of a heterojunction in a ZnS/CaZnOS particle. The bottom shows a schematic of the crystal structure viewed along the [100] direction of the CaZnOS domain and [211] direction of the ZnS domain. (c) SEM image and corresponding element maps of a representative ZnS/CaZnOS particle (with 1% Mn atoms). (d) Schematic configuration of the ML polymer in combination with ML hybrids and phosphor embedded within an acrylic matrix. (e) Photos of pure 3D-printed polymers under UV light irradiation (365 nm). (f) Digital photograph of the friction-driven ML response of the 3D-printed polymer observed in darkness and in daylight (inset). (g) A schematic configuration of the ML fabric composed of cellulose fibers modified with the ZnS/CaZnOS:Mn^{2+} ML particles. (h) Digital photographs of the knitted fabric made of the ZnS/CaZnOS:Mn^{2+} doped cellulose fabric upon rubbing with a glass rod. Reproduced with permission from (a–c) ref. 93 (copyright 2020, John Wiley and Sons) and (d–h) ref. 94 (copyright 2023, John Wiley and Sons).

membranes can transduce light pulses with low optical power densities to enable overdrive heart pacing and nerve bundle activation leading to skeletal muscle contraction (Fig. 9e and f).

4. Macromanipulation of flexible heterojunctions

The statically programmable flexible heterojunctions above could not be further modified once they were prepared. Apart from bottom-up assembly of flexible heterojunctions, *in situ* generation of flexible heterojunctions has been developed recently. Under external stimuli, such as light, temperature, and mechanical force, these flexible heterojunction materials exhibit reprogrammable characteristics. Macromanipulation allows the creation of controllable heterojunctions with reversible sequences and shapes. Besides, the reversible changes enable the dynamic manipulation of functionalities, which can promote the properties of heterojunctions from static to dynamic modes.

Molecular crystals are composed of individual molecules held together by intermolecular forces such as hydrogen bonding, halogen bonding, and π–π interactions, which enable the dynamic tuning of their optoelectronic properties.[96–99] Various smart actuations of these crystals have been explored through external stimuli, including light, pressure, temperature, and solvents.[100–104] Our group[105] introduced a hydration-mediated approach to create flexible heterojunctions. We selected 2-(3-pyridyl)benzimidazole (3Py) due to its nitrogen-rich structures and aromatic rings. The hydrated crystals Py-1 (Fig. 10a) were synthesized through a straightforward solvothermal reaction between 3Py and water at 100 °C and exhibit deep-blue delayed fluorescence. The synthesized Py-1 crystals demonstrate elastic bending. When subjected to excessive bending, the crystal experiences plastic deformation. The notable mechanical flexibility may benefit from the π⋯π interactions and hydrogen bonds as a crucial buffering system. Upon UV irradiation for 10 min, Py-1 crystals exhibited a sky-blue emission. Single-crystal X-ray diffraction analysis suggests the generation of Py-2 with sky-blue emission, indicating that some water is partially released in Py-2 ($3Py \cdot 2.4H_2O$) compared to Py-1 ($3Py \cdot 4H_2O$). SEM indicates that the phase transformation begins at the surface and then occurs homogeneously throughout the crystal. Py-1 displays defect-free single crystals with high crystallinity and smooth surfaces, whereas Py-2 exhibits a rough texture and numerous individual nanostructures (Fig. 10b). By taking advantage of the switchable shape and color-tunable dual emission properties of Py-1, we explored the *in situ* formation of flexible microwire heterojunctions. Irradiating the individual Py-1 microwires for varying

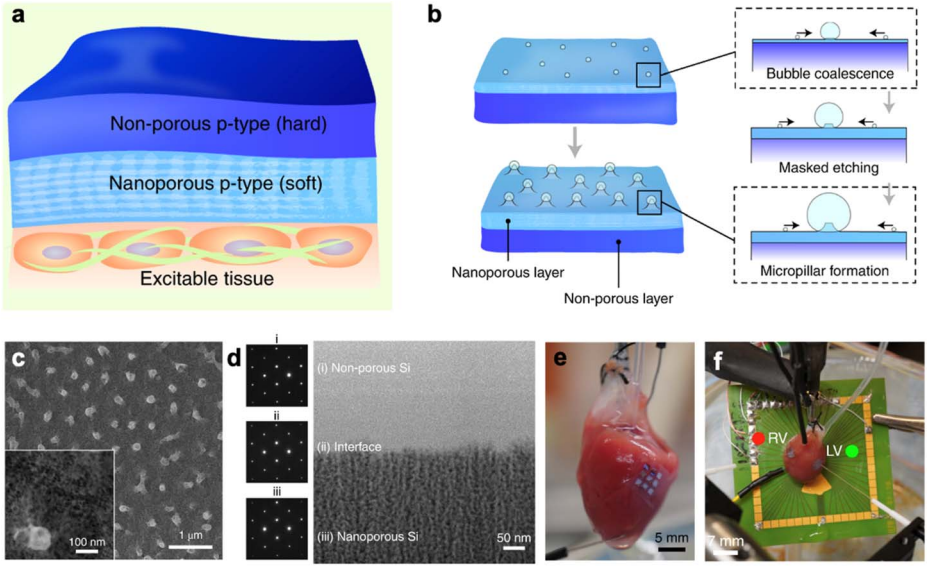

Fig. 9 (a) Schematic representation of a nanoporous/non-porous, soft–hard heterojunction in p-type silicon. (b) Formation of micropillars can be attributed to the coalescence of hydrogen bubbles during wet etching. The schematic presents the proposed model of self-masking leading to pillar formation. (c) A scanning electron microscopy image showing porosification of the material surface and formation of microscale pillars. The inset shows a porous surface. (d) A STEM image showing the interface between the non-porous and nanoporous silicon in the material. Selected area electron diffraction patterns obtained on different material domains and along the [110] zone axis show the same crystalline diffraction pattern and no signs of amorphization. (e) Photograph of the membrane attached to the heart on the left ventricular wall. (f) Photographs of the fibre set-up and microelectrode array used in the dual chamber pacing experiments. A 532 nm laser (4 mW mm^{-2}) was used to stimulate the left ventricle (LV) and an 808 nm laser (60 mW mm^{-2}) was used to stimulate the right ventricle (RV). Reproduced with permission from (a–f) ref. 95 (copyright 2022, Springer Nature).

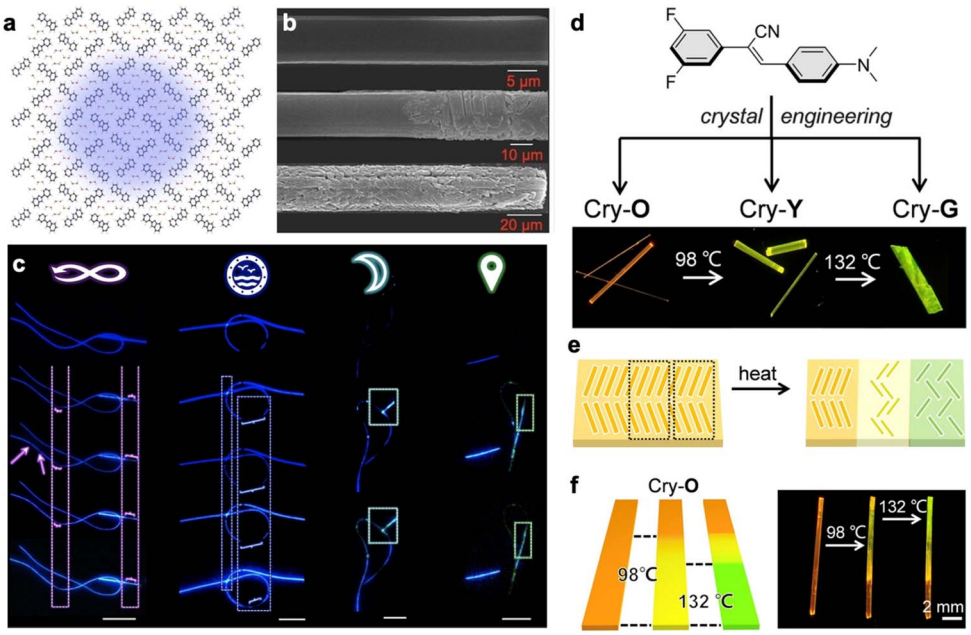

Fig. 10 (a) Molecular packing structure of Py-1 viewed along the crystallographic *a*-axis. (b) SEM images of Py-1, heterojunctions of Py-1 and Py-2, and Py-2, arranged from top to bottom. (c) Continuous dynamic photonic communication system utilizing Py-1 in various shapes (scale bar: 50 μm). (d) The growth and transformation of different crystalline phases. (e) A schematic of the fabrication of ternary pseudo-heterojunctions by heating. (f) Schematic diagram of the phase transitions of Cry-O heated at different parts with different temperatures and the ternary pseudo-heterojunction of Cry-O, which was modified into three different crystal phases by temperature control. Reproduced with permission from (a–c) ref. 105 (copyright 2024, John Wiley and Sons) and (d–f) ref. 106 (copyright 2025, John Wiley and Sons).

durations dramatically alters their emission modes. Simple region-selective hydration treatment of Py-2 facilitates the creation of dynamic and reversible optical junctions. Our versatile water-mediated method allows for the manipulation of various starting materials to achieve light signal modulation (Fig. 10c). The adjustable shapes and color-tunable dual emissions offer thousands of combinations that align precisely in a one-to-one correspondence, making counterfeiting the pattern akin to finding a needle in a haystack. Consequently, true and false information can be effectively transmitted by manipulating the reversible luminescence of the flexible microwires.

Beyond photochromism and hydration-induced luminescence, thermal response has been widely implemented in organic crystal hybrids to enable rapid, remotely triggered actuation. Zhang *et al.*[106] prepared ternary pseudo-heterojunctions through sequential phase transitions upon heating to 98 and 132 °C. DPDAPA (which is (*Z*)-2-(3,5-difluorophenyl)-3-(4-(dimethylamino)phenyl)acrylonitrile) crystals were grown by the solvent diffusion method using dichloromethane as a good solvent and ethanol or petroleum ether as a poor solvent. After about 5 days, thin orange ribbon crystals Cry-O were obtained in a test tube with ethanol as a poor solvent, while fine rod-like yellow crystals Cry-Y formed in the test tube with petroleum ether as a poor solvent. Cry-O demonstrated orange emission and excellent elasticity, whereas Cry-Y emitted yellow fluorescence and rigidity. The parallel arrangement, the interlayer hydrogen bonds and weak π···π interactions allow molecular adjustments under external stress, imparting elastic flexibility to Cry-O. Furthermore, upon heating Cry-O to 98 °C, its fluorescence shifted from orange to yellow, and further heating Cry-O to 132 °C induced a second shift from yellow to green (Fig. 10d). ^{1}H NMR and powder X-ray diffraction analyses confirm a sequential phase transition of Cry-O, initially converting to Cry-Y, followed by a final transformation into Cry-G (Fig. 10e). Leveraging the unidirectional, irreversible phase transitions of Cry-O and Cry-Y, they designed ternary pseudo-heterojunctions through selectively thermal-annealing different parts of the pristine crystals. Specifically, they thermally processed a Cry-O crystal by sequentially heating two-thirds to 98 °C (inducing an intermediate phase) and subsequently one sub-portion to 132 °C, resulting in a ternary pseudo-heterojunction structure with three interconnected phases within a single crystal (Fig. 10f).

5. Summary and outlook

In this perspective, we provide a comprehensive analysis of the burgeoning research field of flexible heterojunctions from the following four points: (1) Flexible heterojunctions at the molecular scale: we introduce intrinsically flexible heterojunctions that are inherently flexible and structurally flexible heterojunctions that are acquired to be flexible. (2) Bottom-up assembly of flexible heterojunctions—a static programmable perspective: we discuss the key developments in self-assembly and stepwise layer-by-layer assembly of flexible heterojunctions including intrinsically flexible heterojunctions and structurally flexible heterojunctions. (3) Manipulation of flexible heterojunctions from a dynamic reprogrammable perspective: we highlight the representative studies on the fabrication of stimuli-responsive flexible crystal-based heterojunctions. (4) Representative optoelectronic applications at the macroscale: the unique combination of mechanical compliance and optical, electronic and other functional properties favors flexible heterojunctions for diverse applications, including sensing, flexible photonics and wearable devices. In summary, the emerging flexible heterojunctions provide an excellent platform and a new opportunity for next-generation optoelectronic integrated circuits.

The synthesis of high-quality flexible heterojunctions is driven by the pursuit of a dual enhancement in both optoelectronic and flexible properties, ultimately paving the way for a wide range of applications. Given the advantages and disadvantages of different existing synthetic methods (including liquid assembly, polymerization, epitaxial growth, exfoliation and transfer, coating and macromanipulation), we can select different methods based on the desired properties and assembly materials.

Looking forward to advancing the generation of flexible heterojunctions, the following challenges need to be considered: (1) developing facile and universal fabrication methods: although the ability to assemble individual building blocks into flexible heterojunctions has been developed in laboratory-scale fabrication, scalable integration of flexible heterojunction devices for large-scale production remains a major challenge. The facile and universal fabrication of flexible heterojunctions with high uniformity and precise control of sequences requires efforts from multiple disciplines. (2) The structure–property relationship: due to the limited number and variety of available flexible heterojunctions, the structure–property relationships guiding the design of basic units for target flexible heterojunctions remain unclear. We propose the application of machine learning methods to predict the dynamic properties of molecules and to assess their flexibility and optoelectronic properties for the target synthesis of flexible heterojunctions. (3) The combination of mechanical compliance and optoelectronic properties: this can be achieved by engineering flexibility and optoelectronic properties into sophisticated heterojunctions, which often surpass those of their single components and even produce novel properties. However, the newly realized mechanical flexibility of heterojunctions suffers from limited applications. The development of flexible integration technologies becomes highly desirable accordingly. Besides, bottom-up assembly of flexible heterojunctions merges the elegance of chemistry with the resilience of engineering, while flexible materials responsive to stimuli are crucial for *in situ* generation of flexible heterojunctions. To draw on the advantages from the two strategies, conducting molecular-level geometric design may explore a brand-new pathway to developing functional flexible heterojunctions. One promising synthetic method is to dope stimuli-responsive molecular materials into flexible matrices and utilize their stimuli-responsive properties for *in situ* generation of flexible heterojunctions. It promises a future

where devices form, adapt, and repair like living tissues. This direction continues in our lab and many others worldwide.

Author contributions

Prof. Dongpeng Yan conceived the project. Meiqi Dai performed the literature search, analyzed the published results, and wrote the manuscript. Prof. Dongpeng Yan revised and supervised the manuscript.

Conflicts of interest

There are no conflicts to declare.

Data availability

No primary research results, software or code have been included and no new data were generated or analysed as part of this perspective.

Acknowledgements

DY is grateful for the kind invitation from the editor's office to provide this contribution. This work was supported by the National Key R&D Program of China (Grant No. 2024YFA1211600), the Scientific Research Innovation Capability Support Project for Young Faculty (ZYGXQNJSKYCXNLZCXM-M3), the National Natural Science Foundation of China (Grant No. 22275021 and W2441007), the Beijing Municipal Natural Science Foundation (Grant No. L234064 and 25JL003), the Beijing Nova Program (Grant No. 20230484414), and the Fundamental Research Funds for the Central Universities.

Notes and references

1 K. Chen, H. Hu, I. H. Song, H. B. Gobeze, W. J. Lee, A. Abtahi, K. S. Schanze and J. G. Mei, *Nat. Photonics*, 2023, **17**, 629–637.
2 Y. Z. Zhang, Y. J. Wang, L. C. Zhao, X. Y. Yang, C. H. Hou, J. Wu, R. Su, S. Jia, J. J. Shyue, D. Y. Luo, P. Chen, M. T. Yu, Q. Y. Li, L. Li, Q. H. Gong and R. Zhu, *Energy Environ. Sci.*, 2021, **14**, 6526–6535.
3 H. Lin, M. Yang, X. N. Ru, G. S. Wang, S. Yin, F. G. Peng, C. J. Hong, M. H. Qu, J. X. Lu, L. Fang, C. Han, P. Procel, O. Isabella, P. Q. Gao, Z. G. Li and X. X. Xu, *Nat. Energy*, 2023, **8**, 789–799.
4 F. Sahli, J. Werner, B. A. Kamino, M. Bräuninger, R. Monnard, B. Paviet-Salomon, L. Barraud, L. Ding, J. J. D. Leon, D. Sacchetto, G. Cattaneo, M. Despeisse, M. Boccard, S. Nicolay, Q. Jeangros, B. Niesen and C. Ballif, *Nat. Mater.*, 2018, **17**, 820–826.
5 Z. J. Xie, B. Zhang, Y. Q. Ge, Y. Zhu, G. H. Nie, Y. F. Song, C. K. Lim, H. Zhang and P. N. Prasad, *Chem. Rev.*, 2022, **122**, 1127–1207.
6 Y. X. Ma, J. Yang, S. H. Chen, H. T. Lin, C. C. Yan, S. P. Zhuo and X. D. Wang, *Matter*, 2022, **5**, 3706–3739.
7 A. Dhakshinamoorthy, Z. H. Li, S. H. Yang and H. Garcia, *Chem. Soc. Rev.*, 2024, **53**, 3002–3035.
8 H. C. Li, Z. Wang, Y. L. Zhao, D. C. Geng, D. Y. Ji and W. P. Hu, *Adv. Devices Instrum.*, 2025, **6**, 0069.
9 J. Royakkers, H. B. Yang, A. J. Gillett, F. Eisner, P. Ghosh, D. G. Congrave, M. Azzouzi, Z. Andaji-Garmaroudi, A. Leventis, A. K. Rao, J. M. Frost, J. Nelson and H. Bronstein, *Nat. Chem.*, 2024, **16**, 1453–1461.
10 S. Padgaonkar, J. N. Olding, L. J. Lauhon, M. C. Hersam and E. A. Weiss, *Acc. Chem. Res.*, 2020, **53**, 763–772.
11 X. D. Wang, Y. H. Huang, J. F. Liao, Y. Jiang, L. Zhou, X. Y. Zhang, H. Y. Chen and D. B. Kuang, *J. Am. Chem. Soc.*, 2019, **141**, 13434–13441.
12 G. Liu, L. Ma, L. C. Yin, G. D. Wan, H. Z. Zhu, C. Zhen, Y. Q. Yang, Y. Liang, J. Tan and H. M. Cheng, *Joule*, 2018, **2**, 1095–1107.
13 G. D. Xue, B. Qin, C. J. Ma, P. Yin, C. Liu and K. H. Liu, *Chem. Rev.*, 2024, **124**, 9785–9865.
14 T. Y. Zhang, J. T. Wang, P. Wu, A. Y. Lu and J. Kong, *Nat. Rev. Mater.*, 2023, **8**, 799–821.
15 Q. Lv, X. D. Wang, Y. Yu, C. F. Xu, Y. J. Yu, X. Y. Xia, M. Zheng and L. S. Liao, *Nat. Chem.*, 2024, **16**, 201–209.
16 Q. Zhang, M. H. Li, L. Li, D. C. Geng, W. Chen and W. P. Hu, *Chem. Soc. Rev.*, 2024, **53**, 3096–3133.
17 X. Wu, B. Li, Z. L. Zhu, C. C. Chueh and A. K. Y. Jen, *Chem. Soc. Rev.*, 2021, **50**, 13090–13128.
18 H. W. Huang, D. Verhaeghe, B. Weng, B. Ghosh, H. W. Zhang, J. Hofkens, J. A. Steele and M. B. J. Roeffaers, *Angew. Chem., Int. Ed.*, 2022, **61**, e202203261.
19 T. Y. Wang, W. Q. Deng, J. P. Cao and F. Yan, *Adv. Energy Mater.*, 2023, **13**, 2201436.
20 Y. Wang, D. X. Zheng, K. Wang, Q. Yang, J. Qian, J. J. Zhou, S. Z. Liu and D. Yang, *Angew. Chem., Int. Ed.*, 2024, **63**, e202405878.
21 A. K. Geim and I. V. Grigorieva, *Nature*, 2013, **499**, 419–425.
22 G. H. Lee, Y. Lee, H. Seo, K. Jo, J. Yeo, S. Kim, J. Y. Bae, C. Kim, C. Majidi, J. Kang, S. K. Kang, S. Ryu and S. Park, *Nat. Commun.*, 2025, **16**, 4320.
23 Y. Cai, J. Shen, C. W. Yang, Y. Wan, H. L. Tang, A. A. Aljarb, C. Chen, J. H. Fu, X. Wei, K. W. Huang, Y. Han, S. J. Jonas, X. Dong and V. Tung, *Sci. Adv.*, 2020, **6**, abb5367.
24 Y. X. Gao, F. L. Deng, R. He and Z. C. Zhong, *Nat. Commun.*, 2025, **16**, 717.
25 W. Zhang, W. S. Jin, T. Fukushima, A. Saeki, S. Seki and T. Aida, *Science*, 2011, **334**, 340–343.
26 T. Zhong, F. Guo, S. Y. Lei, B. Xiao, Q. D. Li, T. Jia, X. C. Wang and R. Q. Yang, *npj Flexible Electron.*, 2023, **7**, 2.
27 Y. Li, L. Meng, Y. M. Yang, G. Xu, Z. Hong, Q. Chen, J. You, G. Li, Y. Yang and Y. Li, *Nat. Commun.*, 2016, **7**, 10214.
28 J. F. Liao, W. Q. Wu, Y. Jiang, J. X. Zhong, L. Wang and D. B. Kuang, *Chem. Soc. Rev.*, 2020, **49**, 354–381.
29 Y. Y. Peng, J. F. Lu, X. D. Wang, W. D. Ma, M. L. Que, Q. S. Chen, F. T. Li, X. H. Liu, W. C. Gao and C. F. Pan, *Nano Energy*, 2022, **94**, 106945.
30 T. Carey, S. Cacovich, G. Divitini, J. Ren, A. Mansouri, J. M. Kim, C. Wang, C. Ducati, R. Sordan and F. Torrisi, *Nat. Commun.*, 2017, **8**, 1202.

31 C. X. Wei, L. Li, Y. Y. Zheng, L. Z. Wang, J. Y. Ma, M. Xu, J. Y. Lin, L. H. Xie, P. Naumov, X. H. Ding, Q. Y. Feng and W. Huang, *Chem. Soc. Rev.*, 2024, **53**, 3687–3713.
32 Z. Lin, Y. Liu, U. Halim, M. Ding, Y. Liu, Y. Wang, C. Jia, P. Chen, X. Duan, C. Wang, F. Song, M. Li, C. Wan, Y. Huang and X. Duan, *Nature*, 2018, **562**, 254–258.
33 Y. J. Tan, H. Godaba, G. Chen, S. T. M. Tan, G. Wan, G. Li, P. M. Lee, Y. Cai, S. Li, R. F. Shepherd, J. S. Ho and B. C. K. Tee, *Nat. Mater.*, 2020, **19**, 182–188.
34 X. Zhang, J. Grajal, J. L. Vazquez-Roy, U. Radhakrishna, X. Wang, W. Chern, L. Zhou, Y. Lin, P. C. Shen, X. Ji, X. Ling, A. Zubair, Y. Zhang, H. Wang, M. Dubey, J. Kong, M. Dresselhaus and T. Palacios, *Nature*, 2019, **566**, 368–372.
35 S. Choi, H. Lee, R. Ghaffari, T. Hyeon and D. H. Kim, *Adv. Mater.*, 2016, **28**, 4203–4218.
36 X. S. Yang, M. B. Al-Handawi, L. Li, P. Naumov and H. Y. Zhang, *Chem. Sci.*, 2024, **15**, 2684–2696.
37 C. Xu, Y. Chen, S. Zhao, D. Li, X. Tang, H. Zhang, J. Huang, Z. Guo and W. Liu, *Chem. Rev.*, 2024, **124**, 10435–10508.
38 A. R. Huang, Y. Y. Fan, K. Wang, Z. Z. Wang, X. Y. Wang, K. Chang, Y. Gao, M. Z. Chen, Q. Q. Li and Z. Li, *Adv. Mater.*, 2023, **35**, 2209166.
39 Q. Zhang, M. A. Screen, L. Bowen, Y. S. Xu, X. Y. Zhang and J. W. Steed, *Chem. Sci.*, 2025, **16**, 7459–7466.
40 X. S. Yang, L. F. Lan, L. Li, X. K. Liu, P. Naumov and H. Y. Zhang, *Nat. Commun.*, 2022, **13**, 2322.
41 L. F. Lan, X. S. Yang, B. L. Tang, X. Yu, X. K. Liu, L. Li, P. Naumov and H. Y. Zhang, *Angew. Chem., Int. Ed.*, 2022, **61**, e202200196.
42 C. H. Zhang and Y. S. Zhao, *Adv. Mater.*, 2024, 2415856, DOI: **10.1002/adma.202415856**.
43 P. Le Floch, S. Zhao, R. Liu, N. Molinari, E. Medina, H. Shen, Z. Wang, J. Kim, H. Sheng, S. Partarrieu, W. Wang, C. Sessler, G. Zhang, H. Park, X. Gong, A. Spencer, J. Lee, T. Ye, X. Tang, X. Wang, K. Bertoldi, N. Lu, B. Kozinsky, Z. Suo and J. Liu, *Nat. Nanotechnol.*, 2024, **19**, 319–329.
44 S. Jiang, J. Liu, W. Xiong, Z. Yang, L. Yin, K. Li and Y. Huang, *Adv. Mater.*, 2022, **34**, e2204091.
45 X. Xu, Y. Wang, D. Liu, X. Yang, Y. Lu, P. Jiang and X. Wang, *Adv. Mater.*, 2024, **36**, 2404469.
46 R. Ghosh, B. Papnai, Y. S. Chen, K. Yadav, R. Sankar, Y. P. Hsieh, M. Hofmann and Y. F. Chen, *Adv. Mater.*, 2023, **35**, 2210746.
47 R. J. Luo, Q. F. Guo, Z. H. Tang, M. M. Zhang, X. X. Li, B. Gao, X. M. Zhang, K. F. Huo and Y. Zheng, *Adv. Funct. Mater.*, 2023, **33**, 2306115.
48 Y. Jiang, H. Y. Chen, J. Y. Li, J. F. Liao, H. H. Zhang, X. D. Wang and D. B. Kuang, *Adv. Funct. Mater.*, 2020, **30**, 2004293.
49 L. Mao, T. Yang, H. Zhang, J. H. Shi, Y. C. Hu, P. Zeng, F. M. Li, J. Gong, X. Y. Fang, Y. Q. Sun, X. C. Liu, J. L. Du, A. J. Han, L. P. Zhang, W. Z. Liu, F. Y. Meng, X. D. Cui, Z. X. Liu and M. Z. Liu, *Adv. Mater.*, 2022, **34**, 2206193.
50 K. L. Wang, Y. Yang, S. Farhan, Y. Wu and W. F. Lin, *Chem. Eng. J.*, 2024, **490**, 151408.
51 S. H. Fan, Q. Yang, G. L. Yin, X. S. Qi, Y. Y. Feng, J. F. Ding, Q. Peng, Y. P. Qu, Q. L. Wang, Y. Shen, M. K. Wang and X. Gong, *Small*, 2024, **20**, 2311978.
52 Y. Li, C. Zhang, T. T. Zhuang, Y. Lin, J. Tian, X. Y. Qi, X. F. Li, R. Wang, L. Wu, G. Q. Liu, T. Ma, Z. He, H. B. Sun, F. J. Fan, H. M. Zhu and S. H. Yu, *J. Am. Chem. Soc.*, 2021, **143**, 7013–7020.
53 W. H. Shao, J. H. Kim, J. Simon, Z. C. Nian, S. D. Baek, Y. Lu, C. B. Fruhling, H. J. Yang, K. Wang, J. Y. Park, L. B. Huang, Y. Yu, A. Boltasseva, B. M. Savoie, V. M. Shalaev and L. T. Dou, *Science*, 2024, **384**, 1000–1006.
54 X. S. Yang, B. Y. Gao, Y. Liu, B. L. Tang, H. Zhang and H. Y. Zhang, *J. Mater. Chem. C*, 2025, **13**, 6547–6555.
55 H. P. Liu, Z. Q. Lu, Z. L. Zhang, Y. Wang and H. Y. Zhang, *Angew. Chem., Int. Ed.*, 2018, **57**, 8448–8452.
56 G. R. Krishna, R. Devarapalli, G. Lal and C. M. Reddy, *J. Am. Chem. Soc.*, 2016, **138**, 13561–13567.
57 Z. H. Wang, W. Q. Han, B. N. Fu, H. W. Kang, P. X. Cheng, J. J. Guan, Y. S. Zheng, R. C. Shi, J. L. Xu and X. H. Bu, *J. Am. Chem. Soc.*, 2025, **147**, 2766–2775.
58 L. F. Lan, X. H. Pan, P. Commins, L. Li, L. Catalano, D. M. Yan, H. A. Xiong, C. G. Wang, P. Naumov and H. Y. Zhang, *CCS Chem.*, 2025, **7**, 905–917.
59 L. F. Lan, L. Li, C. G. Wang, P. Naumov and H. Y. Zhang, *J. Am. Chem. Soc.*, 2024, **146**, 30529–30538.
60 X. W. Feng, R. Lin, S. Yang, Y. Y. Xu, T. J. Zhang, S. W. Chen, Y. K. Ji, Z. F. Wang, S. W. Chen, C. F. Zhu, Z. H. Gao and Y. S. Zhao, *Angew. Chem., Int. Ed.*, 2023, **62**, e202310263.
61 Z. H. Qi, B. Zhou and D. P. Yan, *Adv. Opt. Mater.*, 2023, **11**, 2200852.
62 E. Shi, B. Yuan, S. B. Shiring, Y. Gao, Akriti, Y. Guo, C. Su, M. Lai, P. Yang, J. Kong, B. M. Savoie, Y. Yu and L. Dou, *Nature*, 2020, **580**, 614–620.
63 K. Wei, T. Zhou, Y. Jiang, C. Sun, Y. Liu, S. Li, S. Liu, X. Fu, C. Hu, S. Tian, Y. Yang, X. Fu, N. AlMasoud, S. M. H. Qaid, M. K. Nazeeruddin, H. Y. Hsu, W. D. Li, J. T. Kim, R. Long, W. Zhang, J. Chen and M. Yuan, *Nature*, 2025, **638**, 949–956.
64 Y. H. Lin, S. Y. Liu and D. P. Yan, *Research*, 2023, **6**, 0259.
65 Y. Li, T. T. Zhuang, F. Fan, O. Voznyy, M. Askerka, H. Zhu, L. Wu, G. Q. Liu, Y. X. Pan, E. H. Sargent and S. H. Yu, *Nat. Commun.*, 2018, **9**, 4947.
66 M. S. Gudiksen, L. J. Lauhon, J. Wang, D. C. Smith and C. M. Lieber, *Nature*, 2002, **415**, 617–620.
67 Q. X. Chen, Y. Y. Lu, Y. Yang, L. G. Chang, Y. Li, Y. Yang, Z. He, J. W. Liu, Y. Ni and S. H. Yu, *Nat. Commun.*, 2024, **15**, 3208.
68 B. L. Yuan, B. Yang, P. Xu and M. Y. Zhang, *ACS Nano*, 2025, **19**, 1981–2012.
69 G. Y. Chen, Z. W. Yang, H. Y. Pan, J. Zhang, Y. Guo, Z. Y. Zhou, J. H. Zheng, Z. Q. Zhang, R. Cao, K. Hou and M. F. Zhu, *Chem. Rev.*, 2025, **125**, 5991–6056.
70 W. L. Song, Y. Zhang, C. H. Tran, H. Choi, D. G. Yu and I. Kim, *Prog. Polym. Sci.*, 2023, **142**, 101691.
71 M. Q. Du, H. A. Houck, Q. Yin, Y. W. Xu, Y. Huang, Y. Lan, L. Yang, F. E. Du Prez and G. J. Chang, *Nat. Commun.*, 2022, **13**, 3231.

72 S. Maes, N. Badi, J. M. Winne and F. E. D. Prez, *Nat. Rev. Chem.*, 2025, **9**, 144–158.
73 Z. Huang, X. Chen, S. J. K. O'Neill, G. Wu, D. J. Whitaker, J. Li, J. A. McCune and O. A. Scherman, *Nat. Mater.*, 2022, **21**, 103–109.
74 S. Duan, M. Hua, C. W. Zhang, W. Hong, Y. Yan, A. Jazzar, C. Chen, P. Shi, M. Si, D. Wu, Z. Lin, P. He, Y. Du and X. He, *Chem. Rev.*, 2025, **125**, 7918–7964.
75 D. Y. Wang, J. M. Ding, Y. Q. Mal, C. L. Xu, Z. Y. Li, X. Zhang, Y. Zhao, Y. Zhao, Y. Q. Di, L. Y. Liu, X. J. Dai, Y. Zou, B. Kim, F. J. Zhang, Z. T. Liu, I. McCulloch, M. Lee, C. Chang, X. Yang, D. Wang, D. Q. Zhang, L. D. Zhao, C. A. Di and D. B. Zhu, *Nature*, 2024, **632**, 528–535.
76 S. Wang, H. Feng, B. Li, J. Y. C. Lim, W. Rusli, J. Zhu, N. Hadjichristidis and Z. Li, *J. Am. Chem. Soc.*, 2024, **146**, 16112–16118.
77 Z. H. Zhang, A. K. Biswal, A. Nandi, K. Frost, J. A. Smith, B. H. Nguyen, S. Patel, A. Vashisth and V. Iyer, *Nat. Sustain.*, 2024, **7**, 616–627.
78 J. C. Luo, Z. Demchuk, X. Zhao, T. Saito, M. Tian, A. P. Sokolov and P. F. Cao, *Matter*, 2022, **5**, 1391–1422.
79 K. Yokoyama and Z. B. Guan, *Angew. Chem., Int. Ed.*, 2024, **63**, e202317264.
80 Z. G. Zhao, Z. Q. Cao, Z. X. Wu, W. X. Du, X. Meng, H. W. Chen, Y. C. Wu, L. Jiang and M. J. Liu, *Sci. Adv.*, 2024, **10**, adl2737.
81 F. He, T. Gädt, I. Manners and M. A. Winnik, *J. Am. Chem. Soc.*, 2011, **133**, 9095–9103.
82 B. Adelizzi, A. Aloi, A. J. Markvoort, H. M. M. Ten Eikelder, I. K. Voets, A. R. A. Palmans and E. W. Meijer, *J. Am. Chem. Soc.*, 2018, **140**, 7168–7175.
83 Q. Y. Wan, W. P. To, X. Y. Chang and C. M. Che, *Chem*, 2020, **6**, 945–967.
84 A. Sarkar, R. Sasmal, A. Das, A. Venugopal, S. S. Agasti and S. J. George, *Angew. Chem., Int. Ed.*, 2021, **60**, 18209–18216.
85 Y. Chen, Q. Y. Wan, Y. S. Shi, B. T. Tang, C. M. Che and C. Liu, *Angew. Chem., Int. Ed.*, 2023, **62**, e202312844.
86 A. Sarkar, T. Behera, R. Sasmal, R. Capelli, C. Empereurmot, J. Mahato, S. S. Agasti, G. M. Pavan, A. Chowdhury and S. J. George, *J. Am. Chem. Soc.*, 2020, **142**, 11528–11539.
87 Y. Liu, Y. Huang and X. F. Duan, *Nature*, 2019, **567**, 323–333.
88 Y. Liu, N. O. Weiss, X. D. Duan, H. C. Cheng, Y. Huang and X. F. Duan, *Nat. Rev. Mater.*, 2016, **1**, 16042.
89 Z. J. Huang and D. Shahrjerdi, *Adv. Funct. Mater.*, 2024, **34**, 2314439.
90 I. C. Kwak, J. Kim, J. W. Moon, S. Kim, J. Y. Park, O. K. Song, V. Mazanek, Z. Sofer, H. Jo, S. Y. Park, M. S. Kang, J. Kang and J. H. Cho, *Nat. Electron.*, 2025, **8**, 235–243.
91 Y. H. Yue, G. C. Pan, J. Wan, Z. Xiao, Y. Zhang, S. Q. Xu and G. X. Bai, *Chem. Eng. J.*, 2024, **495**, 153141.
92 Y. K. Li, J. R. Du, X. M. Wang, H. W. Lin and A. Suchocki, *Chem. Eng. J.*, 2025, **512**, 162658.
93 D. F. Peng, Y. Jiang, B. L. Huang, Y. Y. Du, J. X. Zhao, X. Zhang, R. H. Ma, S. Golovynskyi, B. Chen and F. Wang, *Adv. Mater.*, 2020, **32**, 1907747.
94 T. Zheng, M. Runowski, I. R. Martín, K. Soler-Carracedo, L. Peng, M. Skwierczynska, M. Sójka, J. Barzowska, S. Mahlik, H. Hemmerich, F. Rivera-López, P. Kulpinski, V. Lavín, D. Alonso and D. F. Peng, *Adv. Mater.*, 2023, **35**, 2304140.
95 A. Prominski, J. Y. Shi, P. J. Li, J. P. Yue, Y. L. Lin, J. Park, B. Z. Tian and M. Y. Rotenberg, *Nat. Mater.*, 2022, **21**, 647–655.
96 D. K. Bucar, *Nature*, 2024, **630**, 40–41.
97 K. Arora, D. Saini, S. Naskar, S. C. Sahoo, D. Mandal and P. P. Neelakandan, *J. Am. Chem. Soc.*, 2025, **147**, 25498–25507.
98 H. Fang, X. Y. Liu, H. J. Ding, M. Mulcair, B. Space, H. L. Huang, X. W. Li, S. M. Zhang, M. H. Yu, Z. Chang and X. H. Bu, *J. Am. Chem. Soc.*, 2024, **146**, 14357–14367.
99 M. Purdy, J. R. Walton, K. J. Fallon, D. T. W. Toolan, P. Budden, W. X. Zeng, M. K. Corpinot, D. K. Bucar, L. van Turnhout, R. Friend, A. K. Rao and H. Bronstein, *J. Am. Chem. Soc.*, 2023, **145**, 10712–10720.
100 X. H. Pan, L. F. Lan, L. Li, P. Naumov and H. Y. Zhang, *Angew. Chem., Int. Ed.*, 2024, **63**, e202320173.
101 X. H. Pan, L. F. Lan and H. Y. Zhang, *Chem. Sci.*, 2024, **15**, 17444–17452.
102 Q. Di, L. Li, X. D. Miao, L. F. Lan, X. Yu, B. Liu, Y. P. Yi, P. Naumov and H. Y. Zhang, *Nat. Commun.*, 2022, **13**, 5280.
103 Z. L. Xie, X. Y. Zhang, Y. X. Xiao, H. L. Wang, M. Y. Shen, S. M. Zhang, H. D. Sun, R. J. Huang, T. Yu and W. Huang, *Adv. Mater.*, 2023, **35**, 2212273.
104 X. Han, P. X. Cheng, S. S. Han, Z. H. Wang, J. J. Guan, W. Q. Han, R. C. Shi, S. H. Chen, Y. S. Zheng, J. L. Xu and X. H. Bu, *Chem. Sci.*, 2024, **15**, 3530–3538.
105 M. Q. Dai, Z. H. Qi and D. P. Yan, *Angew. Chem., Int. Ed.*, 2025, **64**, 202420139.
106 J. Q. Qi, L. F. Lan and H. Y. Zhang, *Angew. Chem., Int. Ed.*, 2025, **64**, e202500151.